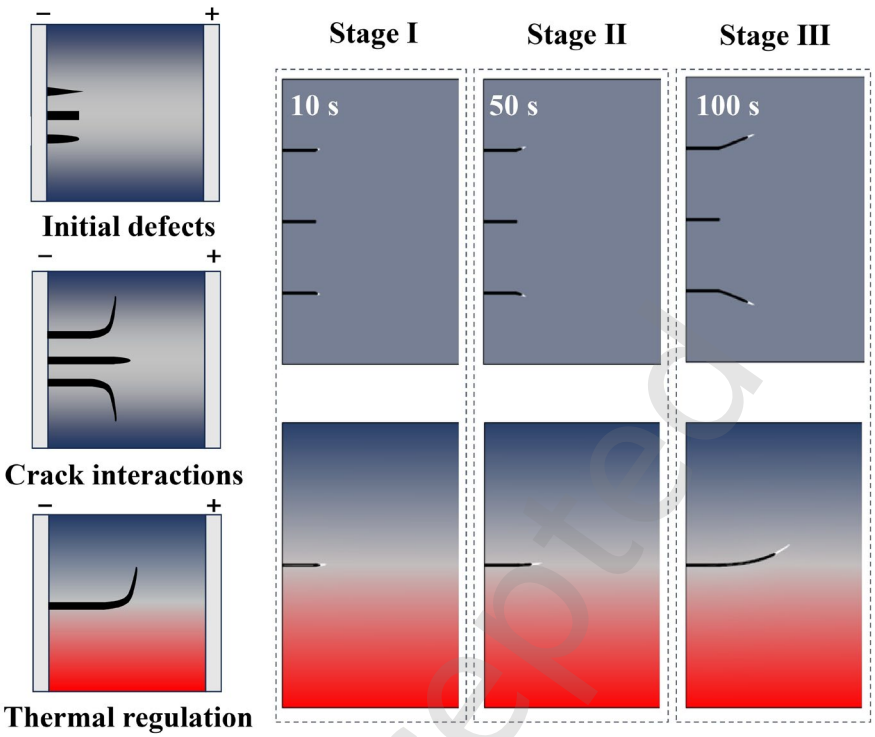
This is a Just Accepted version, keep updated with https://doi.org/10.26599/EMD.2026.9370113
Energy Materials and Devices **2027, 5(1), 9370113**

Graphical Abstract



An electro–chemo–thermal–mechanical phase-field model shows that crack and lithium deposition fronts in solid-state lithium-metal batteries progress from near-stationary behavior through crack-dominated growth to advance at similar speeds. Initial defect shape has the greatest influence at small sizes, while interactions between neighboring cracks can limit propagation and cause outward deflection. Under the simulated thermal conditions, cracks bend toward the colder side, and larger boundary temperature differences are associated with reduced lithium dendrite growth.

Just Accepted

This is a Just Accepted version, keep updated with https://doi.org/10.26599/EMD.2026.9370113
Energy Materials and Devices **2027, 5(1), 9370113**

Research Article

Coordinated crack-dendrite evolution and directional regulation mechanisms in solid state lithium-metal batteries

Junhao Pei[1], Xueshi Bai[1], Yingjun Lei[1], Liang Ma[2], Rui Long[1*], and Zhichun Liu[1]

[1]School of energy and power engineering, Huazhong University of Science and Technology, Wuhan 430074, China

[2]School of Chemistry, Guangzhou Key Laboratory of Materials for Energy Conversion and Storage, South China Normal University, Guangzhou 510006, China

*Address correspondence to Rui Long, r_long@hust.edu.cn

Received: August 27, 2026 / **Revised:** October 16, 2026 / **Accepted:** October 27, 2026

Abstract

Addressing safety issues such as internal short circuits and thermal runaway caused by crack-dendrite co-evolution induced by defects in solid state lithium-metal batteries (SSLMBs), an electro-chemo-thermal-mechanical coupled phase-field model is developed. Impacts of initial crack geometric characteristics, crack number, and intercell temperature gradients on crack propagation and dendrite growth behavior are systematically investigated to reveal the underlying regulatory mechanisms. Results show that effects of initial crack shape on crack propagation and dendrite growth depend on crack size. Among the configurations investigated, the two-crack configuration exhibits the smallest maximum growth distance and pronounced outward crack deflection. At 200 s, its combined crack and dendrite area is approximately 32% smaller than that of the single-crack configuration, while its maximum crack propagation distance decreases from 225.4 to 69.4 μm, a reduction of approximately 69.2%. Interactions between the stress fields of adjacent cracks contribute to this suppression and crack deflection, reducing the risk of short circuits. Temperature heterogeneity across the cell also alters crack propagation paths and dendrite growth patterns. Under large intercell temperature heterogeneities, pronounced crack deflection is accompanied by suppressed dendrite growth. The findings of this study

Just Accepted

provide a rational guidance for SE/anode interface engineering, thermal management strategy developing, thus to regulate directional crack-dendrite co-evolution and upgrade cycle life for SSLMBs.

Keywords: lithium dendrites, cracks, phase field, intercell temperature heterogeneity, solid-state electrolyte

1. Introduction

The growing demand for high-energy-density batteries for electric vehicles and electric vertical takeoff and landing aircraft has increased interest in solid-state lithium-metal batteries (SSLMBs). The ultrahigh theoretical specific capacity and low redox potential (−3.04 V vs. SHE) [1] of lithium metal make SSLMBs promising candidates for next-generation energy storage[2]. SSLMBs offer opportunities to overcome the energy-density and safety limitations of existing lithium-ion batteries [3]. However, lithium dendrite growth, crack propagation, and interfacial instability can occur during charge–discharge cycling [4,5,6]. These coupled processes reinforce one another, leading to internal short circuits, rapid capacity loss, and thermal runaway [7,8,9]. These challenges hinder the large-scale commercial application of SSLMBs [10].

Defects are inevitable in SSLMBs and serve as initiation sites for crack propagation and dendrite growth, strongly affecting long-term battery stability and safety [11,12]. Ning et al. found that dendritic crack initiation and propagation are distinct processes governed by different mechanisms. Crack initiation results from lithium accumulation in subsurface pores, whereas propagation occurs through a wedge-opening mechanism [12]. Crack propagation and lithium dendrite growth exhibit strong mechanical–electrochemical coupling [11,13,14,15]. Initial cracks within the electrode disrupt the interfacial electric and stress fields, concentrating the electric field and stress at crack tips. These local concentrations favor lithium-ion deposition and promote dendrite nucleation and rapid growth [16,17]. Growing dendrites, in turn, generate substantial compressive stress that accelerates crack propagation. This positive feedback between crack propagation and dendrite growth can ultimately cause dendrites to penetrate the separator, resulting in internal short circuits and potentially

Just Accepted

triggering thermal runaway [18,19,20].

In addition to initial crack geometry, crack number is an important defect parameter that affects crack propagation and dendrite growth. In systems with multiple cracks, interactions between the stress fields of adjacent cracks influence crack propagation direction and rate, as well as dendrite growth paths. Crack number and spacing are distinct geometric parameters. When both vary between the configurations investigated, their individual effects on crack propagation and dendrite growth cannot be isolated. Fincher et al. proposed engineering stress in solid electrolytes to deflect dendrites and inhibit further propagation and penetration [21]. Zhang et al. revealed how lithium dendrites mechanically drive fracture in garnet solid electrolytes and proposed grain-boundary toughening and defect engineering as strategies for designing dendrite-resistant solid electrolytes [22]. For all-solid-state sodium batteries, Li et al. developed an interfacial modification strategy in which sodium superionic conductors were co-sintered with a zinc oxide coating to form a conductive composite phase at grain boundaries. This approach improved interfacial ion transport and grain boundary mechanical stability, substantially suppressing sodium dendrite formation and propagation [23].

Lithium-metal batteries also experience spatial temperature variations during operation. Temperature affects ion diffusion in the electrolyte, interfacial electrochemical reaction rates, and stress distributions within the cell. Together, these effects influence crack propagation and dendrite growth, affecting battery service life and safety [24,25]. Temperature can have contrasting effects on lithium dendrite growth depending on the spatial uniformity of the thermal field. Through mesoscale modelling, Vishnugopi et al. showed that a uniform temperature field at approximately 75 °C can suppress dendrite formation through enhanced electrolyte transport and surface self-diffusion. In contrast, localized hotspots can increase the local exchange current density and promote needle-like dendrite growth [26]. Gao and Guo found in phase-field simulations that temperature gradients generated by internal heating can influence the growth direction of lithium dendrites [27]. Yan et al. coupled a nonlinear lithium dendrite phase-field model with a heat-transfer model and demonstrated that

Just Accepted

temperature gradients can suppress lateral dendrite branching [28]. Elevated temperatures can also thicken the solid electrolyte interphase and increase battery impedance; a 50% increase in impedance was reported after aging at 70 °C [29]. Rodrigues et al. noted that, although ceramics have excellent chemical and electrochemical stability, their ability to withstand thermal cycling in batteries remains uncertain. High temperatures combined with large volume changes during lithiation may induce cracks in brittle interfacial layers [30].

Coupled phase-field studies have advanced our understanding of lithium penetration and electrolyte fracture in solid-state batteries. Yuan et al. [13] developed an electrochemical–mechanical phase-field model and demonstrated the effects of defect geometry and stacking pressure on crack propagation and dendrite growth. Bistri and Di Leo [31] formulated a thermodynamically consistent electro-chemo-mechanical gradient theory with separate variables for damage and electrodeposition. Their framework enabled investigations of intergranular and transgranular filament growth and the effects of mechanical confinement. Xue et al. [14] resolved the alternating advance of cracks and lithium dendrites and examined stress-engineering strategies for controlling their propagation. Gao et al. [32] incorporated heat transfer into an electro-chemo-thermo-mechanical framework with independent damage and deposition variables, highlighting the effects of nucleation sites and microstructural heterogeneity. These studies established the capabilities to describe fracture and deposition separately, capture asynchronous crack and deposition front advancement, and account for thermal coupling.

Despite these advances, voids forms as the mismatch of the lithium dendrite evolution and the crack propagation. This mismatch can be significantly impacted by the initial crack geometry, nearby crack-to-crack interaction, and intercell temperature heterogeneity. The underling intrinsic mechanisms under such situations have been not been revealed, such as how initial defect shape and size affect the relative progression of crack propagation and lithium filling; how nonlinear coupling among damage, deposition, and stress in systems with multiple pre-existing cracks influences mutual inhibition and propagation direction; and how spatial temperature variations alter

Just Accepted

coupled evolution through temperature-dependent ion transport, reaction kinetics, and mechanical responses. To address these research gaps, an electro-chemo-thermal-mechanical coupled phase-field model is developed to systematically investigate the influence of initial crack geometric characteristics, crack number, and trans-cell temperature gradients on crack propagation and dendrite growth behavior in solid state lithium-metal batteries. The impacts of these factors on crack propagation rates, the driving forces of dendrite growth, crack deflection angles, and short-circuit risks are systematically analyzed. We elucidate the mechanisms of stress/electric field concentration at the crack tip, the mutual suppression and superposition effects of stresses between cracks, and the intrinsic mechanisms of temperature-enhanced ion transport and interfacial reactions, thereby clarifying the synergistic regulatory mechanisms for crack propagation and dendrite growth. This study may provide a rational guidance for SE/anode interface engineering, thermal management strategy developing, thus to regulate directional crack-dendrite co-evolution and upgrade cycle life for SSLMBs.

2. Materials and Methods

As illustrated in Figure 1, a two-dimensional electro-chemo-thermal-mechanical coupled phase-field model was established to investigate the coordinated evolution behavior of crack propagation and lithium dendrite growth in solid-state lithium-metal batteries, which unifies dendrite phase-field dynamics, crack phase-field evolution, ion transport, charge distribution, elastic deformation and heat transfer within one unified theoretical framework, where two order parameters are adopted to characterize the system state: the dendrite phase-field variable ξ describes the nucleation, growth and morphological evolution of lithium deposition, and the crack phase-field variable d represents crack initiation, propagation, deflection and interaction between multiple cracks. The formulation follows established approaches that describe electrolyte damage and lithium deposition using separate phase-field variables [14,31,32]. In the present implementation, the deposition equation combines interfacial and mechanical contributions with Butler–Volmer kinetics, while a damage-dependent gating function restricts deposition within the electrolyte according to its damage state. The mechanical

Just Accepted

problem includes an overpotential-dependent stress contribution, and crack evolution is driven by the tensile strain-energy history. Thermal effects enter through heat transfer, temperature-dependent diffusion and reaction coefficients, and thermal expansion. This formulation is applied to controlled comparisons of initial crack shape and size, interacting crack configurations, and nonuniform thermal boundary conditions.

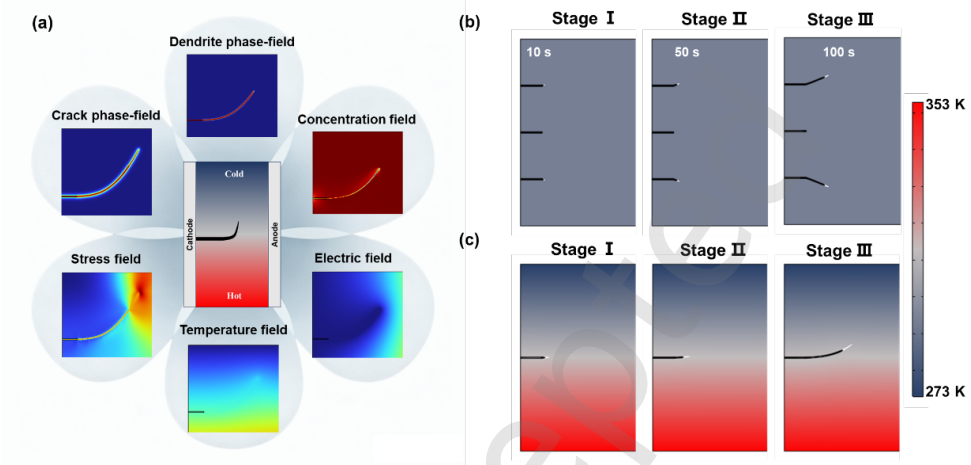


Figure 1. Crack propagation and dendrite evolution based on electro-chemo-thermal-mechanical coupled phase-field model. (a) Schematic of the model framework, showing the coupled fields: dendrite phase-field, crack phase-field, stress field, concentration field, electric potential field, and temperature field. (b) Crack propagation and dendrite evolution with multi-initial defects; (c) Crack propagation and dendrite evolution are characterized by three stages: Stage I (near-stationary crack and lithium fronts), Stage II (crack-dominated propagation), and Stage III (near-synchronous propagation of the crack and lithium fronts).

In the established electro-chemo-thermal-mechanical coupled phase-field model for lithium deposition and crack propagation in the SSLMBs, the Gibbs free energy of the system is expressed as:

$$F = \int_V \left[f_{\text{local}}(\xi) + f_{\text{grad}}(\nabla\xi, \theta) + f_{\text{mech}}(\xi, u_i) \right] dV \quad (1)$$

where $f_{\text{local}}(\xi)$ is the local energy density, $f_{\text{grad}}(\nabla\xi, \theta)$ represents the gradient energy density, and $f_{\text{mech}}(\xi, u_i)$ is the driving force generated by mechanical stress. Here, ξ denotes the phase order parameter of lithium dendrites, with $\xi = 0$ and $\xi = 1$ representing the regions of ungrown and grown dendrites, respectively; d denotes the

phase order parameter of cracks, where $d = 1$ represents the fully fractured region, and $d = 0$ represents the undamaged region. The local energy density is expressed by:

$$f_{\text{local}}(\xi) = \rho\xi^2(1-\xi)^2 \tag{2}$$

where f_{local} represents the double-well potential function, and ρ is the free energy barrier; The equilibrium state lies at the minimum of $f_{\text{local}}(\xi)$, ensuring that both the deposited phase and the undeposited phase are stable. The gradient energy density is given by:

$$f_{\text{grad}}(\nabla\xi, \theta) = \frac{1}{2}\kappa_\xi(\nabla\xi)^2 \tag{3}$$

where κ_ξ represent the surface energy gradient coefficient of the lithium dendrites. The anisotropy of the lithium metal surface energy is given by:

$$\kappa_\xi = \kappa_0[1 + \delta\cos(\omega(\theta - \theta_0))]^2 \tag{4}$$

where κ_0 represents the average surface energy and the interface width, and δ , ω , and $(\theta - \theta_0)$ denote the anisotropy intensity, the crystal symmetry modulus, and the angle between the surface normal migration and the reference axis, respectively.

The driving force induced by mechanical stress, $f_{\text{mech}}(\xi, u_i)$, originates from the strain energy density, which is calculated as

$$\psi = \frac{\lambda\langle \text{tr}^2(\epsilon)\rangle}{2} + \mu\text{tr}(\epsilon^2) \tag{5}$$

where ϵ is the strain tensor; λ and μ are the Lamé coefficients.

The governing equations for phase evolution can be derived from the total energy via the variational method. The evolution for lithium dendrites is described by:

$$\frac{\partial\xi}{\partial t} = f_1(d)\begin{Bmatrix} -L_\sigma^\xi\left(\frac{\partial[f_{\text{local}}(\xi)+f_{\text{mech}}(\xi,u_i)]}{\partial\xi} - \kappa_\xi\nabla^2\xi\right) \\ -L_\eta^\xi h'(\xi)\left\{\exp\left[\frac{(1-\alpha)nF\eta}{RT}\right] - \tilde{c}_+\exp\left[\frac{-\alpha nF\eta}{RT}\right]\right\}\end{Bmatrix} \tag{6}$$

Equation (6) simultaneously accounts for mechanical and electrochemical driving forces, where L_σ^ξ is the interfacial migration coefficient, L_η^ξ represents the electrochemical reaction rate constant, and α is the symmetry factor. $-L_\sigma^\xi\left(\frac{\partial f_{\text{local}}(\xi)}{\partial\xi} - \kappa_\xi\nabla^2\xi\right)$ represents the interfacial driving force provided by the interfacial energy and

Just Accepted

local Gibbs free energy.$-L_\eta^\xi h'(\xi)\left\{\exp\left[\frac{(1-\alpha)nF\eta}{RT}\right]-\tilde{c}_+\exp\left[\frac{-\alpha nF\eta}{RT}\right]\right\}$ is in the form of the Butler-Volmer equation, representing the electrochemical driving force under the overpotential η; The current is confined to the Li/SE interface via the first derivative of the interpolation function $h(x)=x^3(10-15x+6x^2)$ .The step function $f_1(x)$ satisfies $f_1(0)=0$, preventing the formation of lithium dendrites in the solid electrolyte, while $f_1(1)=1$ ensures that lithium metal electrodeposition is unrestricted in regions of the solid electrolyte that are completely damaged.

During the operation of solid-state batteries, lithium ions are considered the only diffusing species in the solid-state electrolyte. The dynamic diffusion process of lithium ions is governed by:

$$\frac{\partial c_+}{\partial t}=\nabla\cdot\left[D^{eff}\nabla c_+ +\frac{D^{eff}}{RT}nF\nabla\varphi\right]-\frac{c_s}{c_0}\frac{\partial\xi}{\partial t} \tag{7}$$

where the first two terms on the right-hand side correspond to the classical Nernst-Planck equation, and the last term represents the deposition term resulting from the reduction of lithium ions in the SE due to the electrochemical deposition process. Here, $D^{eff}=D_{Li}h(\xi)+D_{SE}(1-h(\xi))$ is the effective diffusion coefficient of the system, D_{Li} and D_{SE} are the diffusion coefficients of lithium ions in lithium metal and the SE, respectively; c_s is the number of moles of lithium in the electrode phase; and c_0 is the number of moles of lithium in the solid-state electrolyte.

The electrostatic potential is governed by the Poisson equation

$$\nabla\cdot[\sigma^{eff}\nabla\varphi]=nFc_s\frac{\partial\xi}{\partial t} \tag{8}$$

where $\sigma^{eff}=\sigma_{Li}h(\xi)+\sigma_{SE}(1-h(\xi))$ is the effective conductivity of the system, σ_{Li} and σ_{SE} are the conductivities of the lithium metal and the solid electrolyte, respectively.

The solid mechanics model is introduced to describe the mechanical behavior of the solid-state battery. Following Newton's second law, the governing equations is:

$$0=\nabla_X\cdot F_L(S+S_{ext})+F_V \tag{9}$$

where F_L is the deformation gradient; S is the Piola-Kirchhoff stress tensor; F_V is the volume force; and X is the material coordinates. S_{ext} is the external stress tensor

Just Accepted

caused by local electrochemical overpotential, given by [11,13,33,34]:

$$\sigma_{ij}^{\eta} = \xi \frac{F\eta}{\Omega_{\mathrm{Li}}} \delta_{ij} \tag{10}$$

where Ω_{Li} is the partial molar volume of lithium metal, and δ_{ij} is the Kronecker delta tensor. Material properties within the system, such as mechanical and electrochemical properties including stiffness, electrical conductivity, diffusion coefficient, and density, evolve with the evolution of the phase field. The elastic tensor changes with the evolution of the phase field, expressed as:

$$C_{ijkl}^{eff}(\xi, d) = \left[h(\xi) C_{ijkl}^{Li} + \left(1 - h(\xi)\right) C_{ijkl}^{SE}\right]\left[(1-d)^2 + k\right] + d\xi C_{ijkl}^{Li} \tag{11}$$

where C_{ijkl}^{Li} and C_{ijkl}^{SE} denote the elastic tensors of the lithium dendrites and SEs, respectively, and k is a very small positive constant to ensure computational stability. The effective elastic tensor is zero at $d = 1$ and $\xi = 0$, *i.e.*, the crack surface where no lithium dendrites are present is free. Meanwhile, it ensures that stress is transferred at the Li/SE interface. We decompose the strain energy resulting from elastic deformation into tensile and compressive components [31,35], yielding:

$$\psi_{+} = \frac{\lambda_{\mathrm{eff}} \langle \mathrm{tr}(\boldsymbol{\varepsilon}) \rangle_{+}^{2}}{2} + \mu_{\mathrm{eff}} \mathrm{tr}\left(\boldsymbol{\varepsilon}_{+}^{2}\right) \tag{12}$$

$$\psi_{-} = \frac{\lambda_{\mathrm{eff}} \langle \mathrm{tr}(\boldsymbol{\varepsilon}) \rangle^{2}}{2} + \mu_{\mathrm{eff}} \mathrm{tr}\left(\boldsymbol{\varepsilon}_{-}^{2}\right) \tag{13}$$

where λ_{eff} and μ_{eff} are the effective Lamé constant. The operator symbol $\langle \cdot \rangle$ is defined as: $\langle x \rangle_{\pm} = \frac{x \pm |x|}{2}$. We note that only strain energy caused by tension can drive crack propagation, which prevents damage under compressive stress. The phase-field evolution equation for the crack is as follows [35,36]:

$$\frac{g_c}{l}\left[d - l^2 \Delta d\right] = 2(1-d)H \tag{14}$$

The local history of the maximum positive reference energy is defined as $H(\boldsymbol{x}, t) := \max_{s \in [0,t]} \psi_{+}(\boldsymbol{\varepsilon}(\boldsymbol{x}, s))$ to ensure that the irreversibility constraint holds, and it is contributed solely by the mechanical energy associated with tensile strain. g_c is related to the material fracture energy, and l controls the diffusion length of the fracture region.

In the all-solid-state battery, heat primarily originates from external heat transfer

Just Accepted

and internal heat generation. The temperature evolution for the system is [37]:

$$C_p^{eff}\rho^{eff}\frac{\partial T}{\partial t}=\nabla\kappa^{eff}\nabla T+Q \tag{15}$$

where $C_p^{eff}=C_p^{Li}\left(1-h(\varphi_{cr})\right)+\left(C_p^{Li}h(\xi)+C_p^{SE}\left(1-h(\xi)\right)\right)h(\varphi_{cr})$ is the effective specific heat capacity of the system; C_p^{Li} and C_p^{SE} are the specific heat capacities of the lithium dendrites and the SE, respectively; κ^{eff} is the effective thermal conductivity of the system, which is obtained by interpolation between the thermal conductivity of the lithium dendrites κ_{Li} and the thermal conductivity of the SE κ_{SE}. The heat generation Q primarily consists of Ohmic heat Q_{oh} and polarization heat Q_{op} [38,39]:

$$Q_{oh}=\sigma^{eff}\left(\nabla\varphi\right)^2 \tag{16}$$

$$Q_{op}=a_s\frac{\partial\xi}{\partial t}\varphi \tag{17}$$

where a_s is an empirical factor for converting the theoretical current to the actual current. Temperature affects the diffusion rates of lithium ions in the electrolyte and lithium dendrites, and also influences the electrochemical reaction rate constants, thereby affecting dendrite growth. The specific effects are governed by the Arrhenius empirical equation [39]:

$$D=D_0\exp\left[\frac{-E_d}{R}\left(\frac{1}{T}-\frac{1}{T_0}\right)\right] \tag{18}$$

$$L_\eta^\xi=L_{\eta0}^\xi\exp\left[\frac{-E_a}{R}\left(\frac{1}{T}-\frac{1}{T_0}\right)\right] \tag{19}$$

where D_0 and $L_{\eta0}^\xi$ are the standard diffusion coefficient and standard electrochemical reaction rate constant at temperature T_0, while E_d and E_a represent the energy barriers for lithium-ion diffusion and the electrochemical reaction, respectively. During the real-life operation of solid-state batteries, temperature inhomogeneities induce thermal expansion that impact crack propagation, which in turn affects the growth of lithium dendrites. The strain induced by thermal expansion is given by

$$\varepsilon_{th}=\alpha^{eff}\left(T-T_{ref}\right) \tag{20}$$

Just Accepted

where α^{eff} is the effective thermal expansion coefficient. The thermal expansion model is coupled with the solid mechanics and heat transfer models, and their combined effects influence the system's elastic strain energy density, thereby affecting crack propagation and dendrite growth.

The computational domain was set as 256 μm × 256 μm, consisting of a lithium metal anode and a solid-state electrolyte region, where pre-existing cracks were introduced inside the electrolyte to simulate defect-induced dendrite nucleation. The default initial crack length and width were set to 30 μm and 2 μm, respectively. Detailed material properties and model parameters are provided in the Supporting Information. The axial crack–lithium front separation is defined as $\Delta x = x_c - x_{Li}$, where the front positions are identified using thresholds of $d = 0.5$ and $\xi = 0.5$ and measured along the initial propagation direction from a common origin. This definition is used consistently for straight and deflected paths. For deflected paths, Δx represents the projected separation. In multiple-crack configurations, the crack and lithium fronts are paired within the same branch.

As shown in Figure 1(b), the coupled evolution is characterized by three kinetic stages: an initial near-stationary stage, a crack-dominated propagation stage, and a near-synchronous propagation stage. To quantify these stages, the crack and lithium front velocities, denoted by v_c and v_{Li}, respectively, are obtained by directly differentiating their front positions with respect to time. The velocity ratio is defined as $R = v_c/v_{Li}$.

For each case, the reference velocity, v_{ref}, is defined as the mean of the average crack and lithium front velocities over 150–200 s. Stage I corresponds to negligible front advancement, with both velocities no greater than 10% of v_{ref}. Outside this near-stationary regime, Stage II is characterized by a velocity ratio greater than 1.1, indicating faster crack advancement and increasing front separation. Stage III corresponds to sustained propagation with both velocities greater than 10% of v_{ref} and a velocity ratio between 0.9 and 1.1, indicating approximately equal front velocities and approximately constant separation. The 10% tolerances are adopted as operational criteria for the present analysis. When the lithium front velocity is zero, the velocity

Just Accepted

ratio is undefined, and the individual front velocities are assessed instead. Once the crack extends through the solid electrolyte, the electrolyte loses its bearing capacity, and the stress intensity factor drops rapidly; Meanwhile, lithium dendrites grow much more easily inside the crack than in the intact solid electrolyte, leading to extremely fast Li penetration and short-circuit failure.

3. Results and Discussion

3.1 Effect of initial crack geometry on crack propagation and dendrite evolution

To address the influence of initial defect geometry on crack propagation and dendrite deposition behavior, three kinds of initial crack shapes (rectangular, triangular, and elliptical) with different lengths (L = 10 μm, 20 μm, 30 μm) are considered.

As shown in Figure 2(a), in the early stage of 0-70 s, the crack propagation rate increases significantly as the initial crack length rises, and the nucleation rates of cracks and dendrites accelerate simultaneously. Within this period, the maximum growth distance of the 30 μm crack is approximately 21 times that of the 10 μm crack. The small crack with an initial length of 10 μm evolves slowly, with its overall growth distance below 6 μm in the early phase. After 40 s, the crack propagation rate further increases, and lithium deposition becomes more intense. In the late stage, the final crack lengths reach 108.4 μm and 225.4 μm respectively, presenting a increasement of roughly two times. It indicates that the system evolution is mainly controlled by ion transport and interfacial electrochemical reaction kinetics, and the initial crack size no longer plays a decisive role. Short cracks require more time to build up sufficient local electric field concentration and current density to initiate dendrite deposition and crack propagation. In comparison, electric field concentration readily occurs at the tips of long cracks, enabling local deposition to start earlier and resulting in a faster initial growth rate.

Just Accepted

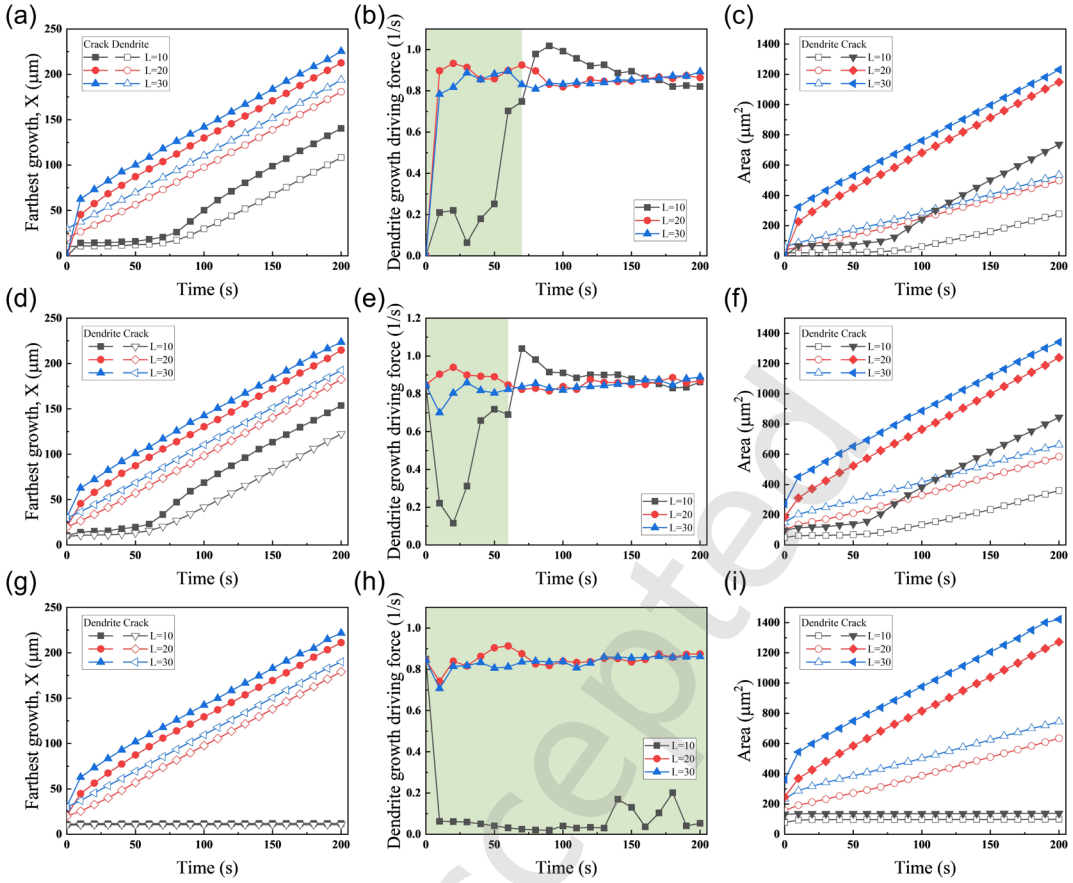


Figure 2. Evolution of the farthest growth distance, dendrite growth driving force, and dendrite/crack area over time for different initial crack lengths (L = 10 μm, 20 μm, 30 μm) under three different initial crack shapes. (a-c) Rectangular crack; (d-f) Triangular crack; (g-i) Elliptical crack. Solid symbols represent crack evolution, while hollow symbols represent dendrite evolution. The green shaded regions in (b), (e), and (h) denote the initial transient growth stage.

The dendrite growth driving force curves further validate the aforementioned stage-specific characteristics (Figure 2 (b, e, h)). During the early deposition phase, lithium dendrite growth rates vary significantly with different initial lengths. Longer initial crack renders higher local deposition rate, accelerating the dendrite deposition process. However, in the later stages, the curves gradually remain relatively stable, indicating that the system enters a transport-reaction coupling control phase, where the influence of geometric size on the overall deposition rate diminishes. For small initial crack sizes, such as L = 10 μm, crack nucleation rate presents a slow value, which

Just Accepted

inhibits dendrite growth, whereas longer cracks provide space for dendrite growth.

For rectangular defects with initial lengths of 10, 20, and 30 μm, the axial front separations are 4.0 μm, 30.8 μm, and 30.6 μm at 50 s and 32.0 μm, 31.8 μm, and 31.6 μm at 200 s, respectively. These results indicate that longer initial defects develop substantial front separation earlier, whereas the three cases retain similar finite separations during late-stage propagation. Thus, approximately matched crack and lithium-front velocities can coexist with a persistent spatial lag.

To quantify the dependence of shape sensitivity on initial defect size, we compare the front positions of rectangular, triangular, and elliptical defects at the same nominal initial length and observation time. The relative spread is defined as $S_q = (X_{q,max} - X_{q,min})/X_{q,max} \times 100\%$, where X_q denotes the crack or lithium-deposition front position measured from the common starting boundary, and the maximum and minimum are taken across the three shapes. Image-derived estimates from Figure 3(d) at 200 s give a crack-front spread of approximately 92%, 9%, and 3% for L = 10 μm, 20 μm, and 30 μm, respectively. The corresponding deposition-front spreads are approximately 91–93%, 10%, and 1–2%. These estimates quantify the contrast in final propagation extent rather than differences in instantaneous growth rates.

The additional insight concerns the size-dependent effectiveness of the prescribed initial shape. At L = 10 μm, the elliptical defect exhibits little front advancement during the observation period, whereas rectangular and triangular defects undergo substantial propagation. At L = 20 and 30 μm, all three shapes propagate appreciably, and their final front positions become much closer. Thus, the influence of initial shape is particularly pronounced in distinguishing near-stationary and propagating behavior for the smallest investigated defects. This observation complements the established trend that longer and sharper defects promote growth by showing that the suppression associated with a smooth initial shape becomes less pronounced in the final propagation extent as the nominal defect length increases[13]. The result is restricted to the investigated geometries, loading conditions, and observation period; it does not establish a universal critical length or a size effect independent of tip sharpness.

The influence of initial defect shape can be interpreted using classical stress-

Just Accepted

concentration and fracture-mechanics arguments. For an elliptical hole in an infinite elastic plate subjected to remote tension perpendicular to its major axis, the Inglis solution gives $K_t = \frac{\sigma_{tip}}{\sigma_0} = 1 + \frac{2a}{b} = 1 + 2\sqrt{\frac{a}{\rho}}$, where a and b are the major and minor semi-axes, respectively, $\rho = b^2/a$ is the tip radius, and σ_0 is the remote tensile stress[40]. At a given defect length, a smaller tip radius therefore produces stronger local stress concentration. The smooth, finite-radius tips of elliptical defects can distribute stress more gradually than the sharp corners of rectangular and triangular defects. The latter can generate more localized stress concentrations, although their actual peak stresses are regularized by the phase-field formulation and spatial resolution.

Stress concentration should be distinguished from the stress intensity factor. For a sharp Mode I crack, $K_I = Y\,\sigma_0\sqrt{\pi\,a}$, where Y accounts for the geometry and loading conditions, and the near-tip stress scales as $\frac{K_I}{\sqrt{2\pi\,r}}$, with r denoting the distance from the tip. These relations provide a mechanical interpretation rather than a quantitative estimate of K_I for the present coupled simulations. In the proposed model, localized tensile stress contributes to the tensile strain-energy history H that drives fracture evolution in Eq. (14). Stronger stress localization can therefore promote damage advancement and facilitate lithium penetration through the damage-dependent deposition coupling. Conversely, weaker localization at a rounded tip is consistent with delayed coupled propagation. Furthermore, at a fixed minor semi-axis, increasing the elliptical defect length decreases its tip radius and increases its stress concentration. Thus, the observed length dependence can reflect changes in both defect extent and tip sharpness.

3.2 Effect of initial crack configurations on crack propagation and dendrite evolution

To investigate the behavior of different initial crack configurations on crack propagation and dendrite growth behavior, a comparative analysis under three initial crack number conditions (N = 1, 2, 3) is conducted. For N = 1 and N = 3, the areas of the dendrites and cracks show no significant variation, and the growth trends remain stable. In contrast, N = 2 yields the smallest areas of dendrites and cracks, and their

Just Accepted

growth rate rises gradually over time. Within the studied simulation duration (0–200 s), the total area of cracks and dendrites for $N = 2$ is roughly 32% lower than that for $N = 1$.

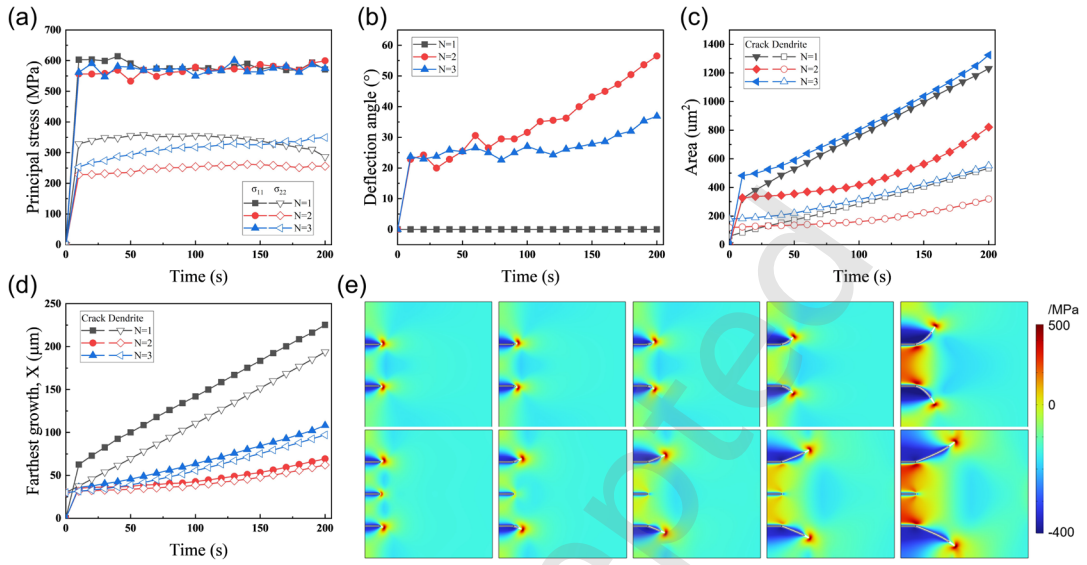


Figure 3 Crack-dendrite coupling evolution for different initial crack numbers ($N = 1$, 2, 3): (a) Temporal evolution of the first and second principal stresses;(b) Temporal evolution of the crack deflection angle; (c) Temporal evolution of the crack/dendrite area; (d) Temporal evolution of the maximum crack/dendrite growth distance; (e) Stress field distribution for N=2 and N=3. Solid symbols represent crack propagation, while hollow symbols represent dendrite evolution.

As shown in Figure 3(ad), for $N = 1$, 2, and 3, the magnitude of the first principal stress is almost identical, with a steady value around 590 MPa. However, as shown in Figure 3(a), the second principal stress reaches its minimum at $N = 2$ (approximately 210 MPa), which slows down crack propagation and further restrains dendrite growth. For $N = 2$, especially in the later stage (120–200 s), the slope of the area evolution curve is 1.28 times higher than those of single-crack (N=1) and triple-crack (N=3) configurations (Figure 3(c)). Dendrite expansion becomes more prominent in multi-crack configurations. Nevertheless, mutual interactions between adjacent cracks emerge during propagation and produce a self-inhibition effect. This demonstrates that the stress field of multi-crack systems no longer follows simple superposition rules, but presents obvious mutual inhibition and nonlinear coupling characteristics.

Just Accepted

The stress contours provide a mechanical interpretation of the different propagation behaviors. For N = 1, Fig. S12(a) shows an approximately symmetric positive T_{yy} concentration ahead of the advancing tip, consistent with straight propagation. For N = 2, both tips retain positive stress concentrations, while their trajectories progressively turn outward (Fig. 3(e) and Fig. S12(b)). The redistribution of stress around the interacting tips is consistent with a change in the balance between opening and shear contributions to crack advancement, producing lateral steering rather than purely forward propagation.

For N = 3, Fig. S12(c) shows a distinctly different distribution: the positive stress concentration at the central tip progressively weakens, whereas pronounced positive concentrations persist at the two outer tips. The central crack is influenced by neighboring cracks on both sides. Their approximately symmetric arrangement reduces the net lateral steering of the central tip, while the weakening of its positive T_{yy} concentration is consistent with bilateral shielding of its opening drive. In the present model, fracture evolution depends on the tensile strain-energy history H in Eq. (14); such shielding can limit further buildup of the local tensile driving force. The outer tips experience a less symmetric neighborhood and retain tensile stress concentrations, allowing continued damage advancement and coupled lithium penetration. The observed behavior therefore reflects a spatial redistribution of the mechanical driving force among the tips.

The influence of crack interactions on deflection is not necessarily monotonic. Figure 3(b) shows smaller late-stage deflection angles for N = 3 than for N = 2, reaching approximately 37° and 57°, respectively, at 200 s. Together with the persistent outer-tip stress concentrations, this smaller deflection preserves a stronger forward propagation component, consistent with the larger maximum penetration distance in Fig. 3(d). Thus, the closer three-crack arrangement exhibits central shielding without a corresponding increase in outward steering of the active outer cracks.

Different initial crack numbers greatly affect the growth kinetics of cracks and dendrites, as well as the internal short-circuit risk of batteries. Generally, longer cracks make it easier for dendrites to reach the cathode and trigger short circuits. In the time

Just Accepted

range of 0–200 s, both crack and dendrite lengths increase approximately linearly with time. As shown in Figure 3(d), $N = 1$ renders the maximum growth distance, with the final length reaching 225.4 μm, corresponding to the highest short-circuit risk. For $N = 2$, the final length drops to 69.4 μm, a reduction of about 69.21%, which proves an obvious suppression effect. For $N = 3$, the final length is 108.2 μm, and the inhibitory effect is weakened.

The differences among the investigated configurations are associated with interactions between neighboring crack stress fields. In the two-crack configuration, these interactions accompany pronounced outward deflection and a smaller maximum growth distance than in the single- and three-crack configurations (Fig. 3). In the three-crack configuration, propagation of the central crack is suppressed, whereas the two lateral cracks continue to advance, resulting in a larger maximum growth distance than in the two-crack case. These observations demonstrate that crack interactions can modify the coupled propagation paths and growth extent. However, crack number and spacing vary simultaneously in the present comparisons, so their individual contributions cannot be separated. The two-crack configuration therefore exhibits the strongest suppression among the layouts investigated here; this result does not establish an optimal crack spacing or imply that two cracks are generally preferable. Determining an optimal spacing would require an independent spacing study at a fixed crack number.

3.3 Directional regulation of Crack Propagation and Dendrite Evolution via inhomogeneous temperature

To systematically investigate the influence of intercell temperature gradients on the coupled evolution of cracks and dendrites, a non-uniform temperature field is applied parallel to the electrode plane (along the vertical direction in the simulation domain). Here, the temperature at the cold boundary is fixed at $T_0 = 273$ K, while the opposite hot boundary is set to a variable temperature T_1 ($T_1 = 273$ K, 303 K, 333 K, 343 K, and 353 K). Adjusting T_1 yields different intercell temperature gradients, where are defined as $\Delta T = T_1 - T_0$.

Just Accepted

This is a Just Accepted version, keep updated with https://doi.org/10.26599/EMD.2026.9370113
Energy Materials and Devices **2027, 5(1), 9370113**

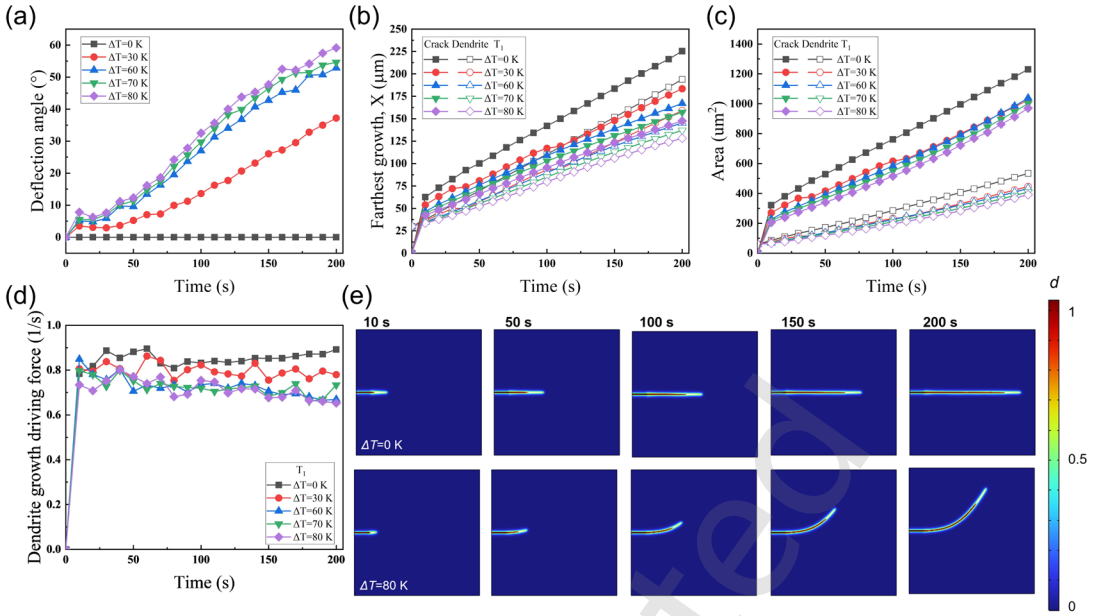


Figure 4 Temporal crack-dendrite coupling evolution under different intercell temperature difference (ΔT = 0 K, 30 K, 60 K, 70 K, 80 K): (a) Temporal evolution of the crack deflection angle;(b) Temporal evolution of the maximum crack/dendrite growth distance; (c) Temporal evolution of the crack/dendrite area; (d) Temporal evolution of the dendrite growth driving force;(e) Dendrite morphology evolution at different time points (10 s, 50 s, 100 s, 150 s, 200 s) under conditions of uniform temperature condition and large temperature gradient ΔT = 80 K). Solid symbols represent crack evolution, while hollow symbols represent dendrite evolution.

Figure 4 illustrates the time-dependent evolution of crack deflection angle, dendrite length, dendrite area, and dendrite growth driving force under different trans-cell temperature gradient, along with stress distributions. The investigated thermal boundary conditions significantly affect crack propagation and dendrite growth kinetics. As shown in Figure 4(a), regarding crack deflection angle, the crack remains at 0° with no deflection under uniform temperature field. As the trans-cell temperature gradient increases, the crack deflection angle exhibits an obvious increase. At ΔT = 80 K, the deflection angle can reach approximately 60° within 200 s, indicating that larger intercell temperature heterogeneity can effectively induce a deviation in the crack propagation path. Meanwhile, larger intercell temperature heterogeneity hinders the evolution of dendrite length and area. For uniform temperature field (ΔT = 0 K), both

Just Accepted

dendrite length and area exhibit largest values, with the dendrite length at approximately 225 μm and the area at approximately 1200 μm² after 200 s (Figure 4(b, c)). At ΔT = 80 K, the dendrite length and area are reduced to approximately 150 μm and 950 μm², respectively.

Under the investigated nonuniform thermal conditions, greater crack deflection is accompanied by reduced dendrite growth, suggesting a lower tendency for lithium penetration toward the cathode. As shown in Figure 4(d), at ΔT = 0 K, the dendrite growth driving force consistently remained at a high level of 0.8–0.9 s^{-1}, sustaining the continuous growth of dendrites. However, at higher intercell temperature heterogeneities, the driving force gradually decrease; At ΔT = 80 K, the dendrite growth driving force is only about 0.6–0.7 s^{-1}, leading to slowed dendrite growth.

For uniform temperature conditions (ΔT = 0 K), the stress field at the crack tip is highly concentrated and distributed along a straight line with no significant deflection, corresponding to rapid dendrite extension along the initial direction and forming a linear growth pattern with high short-circuit risk; Under larger intercell temperature heterogeneity (ΔT = 80 K), the stress fields on both sides of the crack undergo significant redistribution and interference(Figure S15(e)), inducing obvious deflection in the crack propagation direction. The degree of stress concentration at the tip is substantially reduced, thereby weakening the driving force for dendrite growth and suppressing dendrite growth. These observations suggest that nonuniform thermal boundary conditions can modify crack propagation paths and dendrite growth patterns through coupled mechanical and electrochemical responses, providing a potential means of influencing lithium penetration.

Under the investigated thermal boundary conditions, smaller temperature differences are associated with limited crack deflection and a relatively high dendrite growth driving force. Dendrites advance rapidly along the initial direction toward the cathode side, indicating a higher tendency for electrolyte penetration. At larger temperature differences, cracks exhibit pronounced deflection and the dendrite growth driving force decreases, accompanied by suppressed dendrite propagation. These findings suggest that modifying the battery temperature field may provide a route to

Just Accepted

influencing crack–dendrite evolution and inform the development of thermal management strategies for SSLMBs. Since the temperature difference and mean boundary temperature vary simultaneously, the observed behavior reflects their combined influence.

3.4 Effects of thermal kinetics and thermal stress

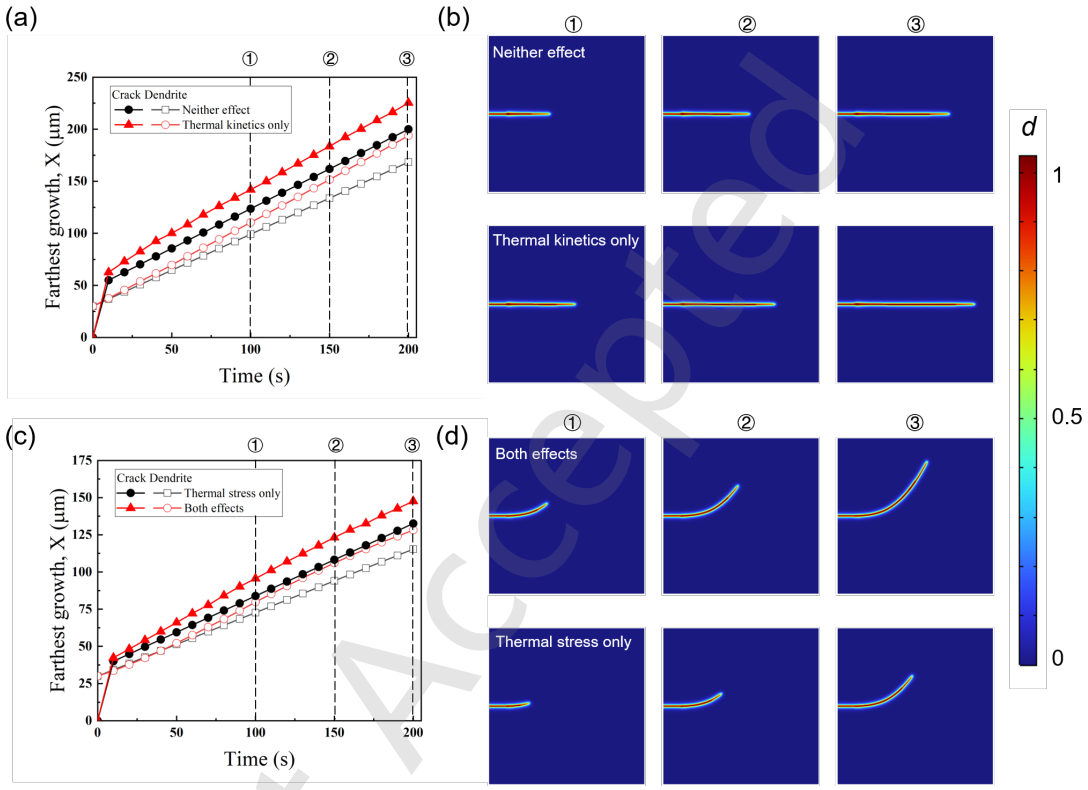


Figure 5. Comparative effects of thermal kinetics and thermal stress on coupled crack propagation and lithium dendrite growth at ΔT = 80 K. (a) Maximum axial crack and lithium-front positions, X (μm), versus time (s) for the cases with neither thermal effect and thermal kinetics only. (b) Corresponding crack phase-field distributions, with neither effect in the upper row and thermal kinetics only in the lower row. (c) Maximum axial crack and lithium-front positions versus time for the cases with thermal stress only and both effects. (d) Corresponding crack phase-field distributions, with both effects in the upper row and thermal stress only in the lower row. The dashed lines marked ①, ② and ③ indicate 100, 150, and 200 s, respectively, corresponding to the snapshot columns from left to right. Solid and open symbols denote crack and lithium fronts, respectively. Thermal stress refers to the mechanical effect induced by thermal

Just Accepted

expansion.

To distinguish the effects of temperature-dependent kinetics and thermal-expansion-induced mechanical coupling, four comparative cases are considered at the same prescribed temperature difference of ΔT = 80 K: neither thermal effect, thermal kinetics only, thermal stress only, and both effects (Fig. 5). The comparison indicates that pronounced crack deflection primarily originates from the mechanical effects induced by thermal expansion. Without thermal-expansion coupling, the cracks propagate approximately along the initial direction, even when temperature-dependent kinetics is activated. Including thermal expansion produces a curved propagation path, consistent with thermal stress modifying the local mechanical driving force for fracture.

Thermal kinetics primarily influences the growth rate of lithium dendrites. Under the investigated conditions, activating temperature-dependent kinetics promotes lithium-front advancement. Faster lithium growth may, in turn, increase the crack propagation rate through electrochemical–mechanical coupling. This indirect influence on crack advancement should be considered together with the directional regulation caused by thermal expansion. At 200 s, the axial crack-front position is approximately 225 μm in the thermal-kinetics-only case and 200 μm when both effects are included, corresponding to a reduction of approximately 11.1%. These results indicate that the combined response reflects the interplay between kinetically promoted lithium growth and mechanically induced crack deflection. The reported reduction refers to penetration along the initial propagation direction.

4. Summary

This study established an electro-chemo-thermal-mechanical coupled phase-field model is developed to address safety issues such as internal short circuits and thermal runaway caused by crack-dendrite co-evolution induced by initial cracks in solid state lithium-metal batteries. The regulatory mechanisms of initial crack geometric characteristics, crack number, and intercell temperature gradients on crack propagation and dendrite growth behavior were systematically investigated.

1. Initial defect geometry affects both the onset and extent of coupled propagation. Longer defects promote earlier crack advancement and lithium deposition. The

Just Accepted

influence of initial shape depends on defect size: small elliptical defects exhibit limited advancement, whereas rectangular and triangular defects propagate more readily. At larger initial lengths, the differences in final propagation extent between the three shapes become less pronounced.

2. Crack interactions redistribute the local mechanical driving force and modify propagation paths. Among the configurations investigated, the two-crack configuration exhibits the smallest maximum growth distance and pronounced outward deflection. At 200 s, its total crack–dendrite area is approximately 32% lower than that of the single-crack configuration. Its maximum crack propagation distance is 69.4 μm, compared with 225.4 μm in the single-crack configuration. In the three-crack configuration, central-crack propagation is suppressed while the lateral cracks continue to advance.

3. Intercell temperature heterogeneities can significantly alter crack propagation paths and dendrite growth patterns. Under small intercell temperature heterogeneities, cracks do not deflect, and dendrites evolution rapidly along a straight line towards to the cathode side; under large intercell temperature heterogeneities, cracks deflect significantly, leading to suppressed dendrite growth, and reduced short-circuit risk. These observations provide mechanistic insights that may inform further studies of SE/anode interface engineering and thermal management.

The present two-dimensional model provides a controlled framework for understanding the coupled effects of defect geometry, crack interactions, and temperature heterogeneity. Its effective continuum description does not explicitly resolve three-dimensional grain structures, grain-boundary effects, or out-of-plane propagation. The simulations focus on prescribed initial defects during charging, while repeated defect formation and interfacial evolution during cycling remain important extensions. Within this scope, the findings may inform interfacial defect control, local stress management, and assessment of thermal conditions. Further development incorporating realistic three-dimensional microstructures, together with operando imaging and cycling experiments, would help establish quantitative design criteria and assess the potential benefits for battery reliability and cycle life.

Just Accepted

Acknowledgments

None.

Author contribution statement

Junhao Pei is responsible for methodology development, software implementation, formal analysis, visualization, and writing the original draft. Xueshi Bai is responsible for validation, formal analysis, and manuscript review and editing. Yingjun Lei is responsible for investigation and manuscript review and editing. Liang Ma is responsible for providing research resources and manuscript review and editing. Rui Long is responsible for conceptualization, supervision, and manuscript review and editing. Zhichun Liu is responsible for supervision and manuscript review and editing. All the authors have approved the final manuscript.

Data availability

The data that support the findings of this study are available from the corresponding author upon reasonable request.

Declaration of competing interest

The authors declare no competing financial interest.

Funding

This work was financially supported by the National Natural Science Foundation of China (Grant No. 52176070), and the Natural Science Foundation of Guangdong Province, China (Grant No. 2024A1515010957).

Use of AI statement

None.

References

[1] Xu, W. *et al.* Lithium metal anodes for rechargeable batteries. *Energy Environ. Sci.* **7**, 513–537 (2014).

[2] Lin, D., *et al*. Reviving the lithium metal anode for high-energy batteries. *Nature Nanotech* **12**, 194–206 (2017).

Just Accepted

[3] Li, J., *et al*. Solid Electrolyte: the Key for High-Voltage Lithium Batteries. *Advanced Energy Materials* **5**, 1401408 (2015).

[4] Huang, W. *et al.* Lithium metal anode: Past, present, and future. *MetalMat* **1**, e6 (2024).

[5] Cheng, X. *et al.* A Review of Solid Electrolyte Interphases on Lithium Metal Anode. *Advanced Science* **3**, 1500213 (2016).

[6] Fincher, C. D. *et al.* Electrochemical corrosion accompanies dendrite growth in solid electrolytes. *Nature* **652**, 906–911 (2026).

[7] Qing Ai. *et al*. ,Strong and brittle lithium dendrites. *Science* **391**,1125-1129(2026).

[8] Kasemchainan, J. *et al.* Critical stripping current leads to dendrite formation on plating in lithium anode solid electrolyte cells. *Nat. Mater.* **18**, 1105–1111 (2019).

[9] Ning, Z. *et al.* Visualizing plating-induced cracking in lithium-anode solid-electrolyte cells. *Nat. Mater.* **20**, 1121–1129 (2021).

[10] Wang, J. *et al.* Challenges and progresses of lithium-metal batteries. *Chemical Engineering Journal* **420**, 129739 (2021).

[11] Porz, L. *et al.* Mechanism of Lithium Metal Penetration through Inorganic Solid Electrolytes. *Advanced Energy Materials.* **7**, 1701003 (2017).

[12] Ning, Z. *et al.* Dendrite initiation and propagation in lithium metal solid-state batteries. *Nature* **618**, 287–293 (2023).

[13] Yuan, C. *et al.* Coupled crack propagation and dendrite growth in solid electrolyte of all-solid-state battery. *Nano Energy* **86**, 106057 (2021).

[14] Xue, D. et al. Dynamic Interplay of Dendrite Growth and Cracking in Lithium Metal Solid-State Batteries. *Journal of the Mechanics and Physics of Solids* **202**, 106197 (2025).

[15] Lewis, J. A., Tippens, J., Cortes, F. J. Q. & McDowell, M. T. Chemo-Mechanical Challenges in Solid-State Batteries. *Trends in Chemistry* **1**, 845–857 (2019).

[16] Bucci, G. & Christensen, J. Modeling of lithium electrodeposition at the lithium/ceramic electrolyte interface: The role of interfacial resistance and surface defects. *Journal of Power Sources* **441**, 227186 (2019).

[17] Gao, X. *et al.* Thermodynamic Understanding of Li-Dendrite Formation. *Joule* **4**, 1864–1879 (2020).

[18] Lai, X. *et al.* Mechanism, modeling, detection, and prevention of the internal short circuit in

Just Accepted

lithium-ion batteries: Recent advances and perspectives. *Energy Storage Materials* **35**, 470–499 (2021).

[19] Cheng, E. J., Sharafi, A. & Sakamoto, J. Intergranular Li metal propagation through polycrystalline Li6.25Al0.25La3Zr2O12 ceramic electrolyte. *Electrochimica Acta* **223**, 85–91 (2017).

[20] LePage, W. S. et al. Lithium Mechanics: Roles of Strain Rate and Temperature and Implications for Lithium Metal Batteries. *J. Electrochem. Soc*. **166**, A89–A97 (2019).

[21] Fincher, C. D. et al. Controlling dendrite propagation in solid-state batteries with engineered stress. *Joule* **6**, 2794–2809 (2022).

[22] Zhang, Y. *et al.* Mechanically driven Li dendrite penetration in garnet solid electrolyte. *Nature* **652**, 912–918 (2026).

[23] Li, B. *et al*. Highly Stable Quasi-Solid-State Sodium Batteries via Facile Grain Boundary Engineering. *ACS Appl. Mater. Interfaces* **18**, 14904–14913 (2026).

[24] Ma, S. *et al.* Temperature effect and thermal impact in lithium-ion batteries: A review. *Progress in Natural Science: Materials International* **28**, 653–666 (2018).

[25] Cao, D. *et al.* Lithium Dendrite in All-Solid-State Batteries: Growth Mechanisms, Suppression Strategies, and Characterizations. *Matter* **3**, 57–94 (2020).

[26] Vishnugopi, B. S., Hao, F., Verma, A., & Mukherjee, P. P. Double-Edged Effect of Temperature on Lithium Dendrites. ACS Applied Materials & Interfaces 12, 23931–23938 (2020).

[27] Gao, L. & Guo, Z. Phase-field simulation of Li dendrites with multiple parameters influence. *Computational Materials Science* **183**, 109919 (2020).

[28] Yan, H. H., Bie, Y. H., Cui, X. Y., Xiong, G. P. & Chen, L. A computational investigation of thermal effect on lithium dendrite growth. *Energy Conversion and Management* **161**, 193–204 (2018).

[29] Waldmann, T., Wilka, M., Kasper, M., Fleischhammer, M. & Wohlfahrt-Mehrens, M. Temperature dependent ageing mechanisms in Lithium-ion batteries – A Post-Mortem study. *Journal of Power Sources* **262**, 129–135 (2014).

[30] Rodrigues, M.-T. F. *et al.* A materials perspective on Li-ion batteries at extreme temperatures. *Nat Energy* **2**, 17108 (2017).

[31] Bistri, D. & Di Leo, C. V. A continuum electro-chemo-mechanical gradient theory coupled with

Just Accepted

damage: Application to Li-metal filament growth in all-solid-state batteries. *Journal of the Mechanics and Physics of Solids* **174**, 105252 (2023).

[32] Gao, X., Zhang, Y. & Liew, K. M. Electro-chemo-thermo-mechanical phase-field model for lithium penetration in solid electrolytes. *International Journal of Mechanical Sciences* **307**, 110913 (2025).

[33] Monismith, S., Fincher, C. D., Chiang, Y., Qu, J. & Dingreville, R. Harnessing Electrochemical-Mechanical Couplings to Improve the Reliability of Solid-State Batteries. *Advanced Energy Materials* **14**, 2303567 (2024).

[34] Yuan, C., Lu, W. & Xu, J. Unlocking the Electrochemical–Mechanical Coupling Behaviors of Dendrite Growth and Crack Propagation in All-Solid-State Batteries. *Advanced Energy Materials* **11**, 2101807 (2021).

[35] Miehe, C., Hofacker, M. & Welschinger, F. A phase field model for rate-independent crack propagation: Robust algorithmic implementation based on operator splits. *Computer Methods in Applied Mechanics and Engineering* **199**, 2765–2778 (2010).

[36] Ambati, M., Gerasimov, T. & De Lorenzis, L. A review on phase-field models of brittle fracture and a new fast hybrid formulation. *Comput Mech* **55**, 383–405 (2015).

[37] Lin, J., Chu, H. N., Howey, D. A. & Monroe, C. W. Multiscale coupling of surface temperature with solid diffusion in large lithium-ion pouch cells. Communications Engineering 1, 1 (2022).

[38] Hao, W., Guo, F., Li, J. & Xie, J. Influence of Physical Parameters on Lithium Dendrite Growth Based on Phase Field Theory. Metals 16, 41 (2026).

[39] Li, Y., Zhao, W., Zhang, G. & Shi, S. Unified Picture on Temperature Dependence of Lithium Dendrite Growth via Phase-Field Simulation. *Energy Material Advances* **4**, 0053 (2023).

[40] Inglis, C. E. Stresses in a plate due to the presence of cracks and sharp corners. *Transactions of the Institution of Naval Architects*. **55**, 219–241 (1913).

Just Accepted